ADVANCED FUNCTIONAL MATERIALS
www.afm-journal.de

Kinetic Insights into Precursor-Assisted Soft Sphere Close Packing Revealed by In Situ GISAXS with Implications for Gas Sensing

Guangjiu Pan, Wenhe Xie, Suzhe Liang, Ting Tian, Shanshan Yin, Lixing Li, Altantulga Buyan-Arivjikh, Jinsheng Zhang, Thomas Baier, Zhuijun Xu, Matthias Schwartzkopf, Sarathlal Koyiloth Vayalil, Stephan V. Roth, Yonghui Deng, and Peter Müller-Buschbaum**

Packing of soft spheres, such as micelles, polymer-grafted particles, and microgels, enables the creation of diverse functional materials. Despite the importance of achieving precise structural control, understanding the kinetics of non-equilibrium packing in a large-scale deposition process remains challenging. This study investigates the kinetics of the precursor-assisted close packing of soft spheres using block copolymer micelles as the sphere model. Adding the inorganic precursor $SnCl_4$ is crucial for achieving the close packing, which is versatile and provides a robust platform for tailoring mesoporous materials with tunable pore sizes. The kinetics of the close-packing process are explored by in situ grazing-incidence small-angle X-ray scattering measurements during slot-die coating. The soft crystallization process shows six distinct stages: dilute dispersion, concentrated dispersion, wet film, structuring wet film, gel film, and glassy film. The close packing develops first in the in-plane direction with rapid domain growth and then advances in the out-of-plane direction. Precursors in the interstitial voids play a key role by mitigating packing frustration and favoring face-centered cubic (FCC) ordering. The structure finally stabilizes into a well-ordered FCC structure with large domain sizes. The derived mesoporous SnO_2 features semiconducting properties and enhanced pore connectivity, thus showing superior gas sensing performance toward ethanol.

1. Introduction

Packing is a fundamental principle in the design and optimization of materials, allowing scientists to engineer structures with novel properties. From the precise arrangement of microelectronic components in chips to the assembly of atoms and molecules into functional materials, the study of packing spans multiple scales and disciplines.[1–5] Among geometrical models, spheres are particularly useful due to their symmetry and simplicity. While hard spheres typically adopt dense arrangements like face-centered cubic (FCC) and hexagonal close packing, the packing preferences of soft spheres, such as micelles, polymer-grafted particles, and liquid crystals, are remarkably different.[6–10] In such systems, body-centered cubic (BCC) packing often dominates, driven by the interplay of configurational entropy and the minimization of free energy within the soft corona.[9–11] Block copolymers (BCPs) in selective solvents or melts undergo microphase separation. They self-assemble into

G. Pan, S. Liang, T. Tian, S. Yin, L. Li, A. Buyan-Arivjikh, J. Zhang, T. Baier, Z. Xu, P. Müller-Buschbaum
Chair for Functional Materials
Department of Physics
TUM School of Natural Sciences
Technical University of Munich
James-Franck-Str. 1, 85748 Garching, Germany
E-mail: muellerb@ph.tum.de

The ORCID identification number(s) for the author(s) of this article can be found under https://doi.org/10.1002/adfm.202505935

DOI: 10.1002/adfm.202505935

W. Xie, Y. Deng
Department of Chemistry
State Key Laboratory of Molecular Engineering of Polymers
Shanghai Key Laboratory of Molecular Catalysis and Innovative Materials
Collaborative Innovation Center of Chemistry for Energy Material (iChEM)
College of Smart Materials and Future Energy
Fudan University
Shanghai 200433, China
E-mail: yhdeng@fudan.edu.cn

S. Liang
Eastern Institute for Advanced Study
Eastern Institute of Technology
Ningbo, Zhejiang 315201, P. R. China

S. Yin
School of Mathematics and Physics
Jiangsu University of Technology
Changzhou 213001, China

micelles, which consist of a dense polymeric core surrounded by a flexible corona, providing an ideal model for investigating the packing of soft spheres.[10,12–14]

Theoretical models, such as the dimensionless ratio λ (the corona-to-core size ratio), provide a framework for predicting the choice of FCC or BCC structures.[6,15,16] Although the thermodynamics and phase diagram of soft sphere packing have been well established, experimental observations often diverge from these predictions, emphasizing the critical role of non-equilibrium factors. Kinetic barriers, solvent residues, and pathway-dependent processes often dictate packing outcomes during deposition.[17–19] During deposition processes, such as solution casting or coating, solvent removal forces micelles into close proximity to fill the voids left by evaporation. This compression causes overlapping of micelle coronas, leading to excess polymer density that must be redistributed into void spaces. The degree of this overlap, the associated free-energy cost, and the resulting packing symmetry are strongly influenced by solvent dynamics and the pathway of structure formation during drying.[9–11] Notably, transformations in packing symmetry during solvent evaporation have been reported in polymer-grafted nanoparticles and analogous systems, highlighting the importance of kinetic effects.[17–19]

The situation becomes even more intricate with the inclusion of inorganic precursors, a common strategy for fabricating mesoporous materials. This strategy has been widely used for the synthesis of various mesoporous materials, including carbon, metals, metal oxides, ceramics, etc.[20–24] These mesoporous materials, templated by BCP micelles, exhibit pore architectures with unique properties that are critical for applications in catalysis, gas separation, energy storage, and biomedicine.[21–23,25] The ability to precisely manipulate the packing of BCP micelles has broad implications for materials science, particularly in the fabrication of mesoporous materials with ordered pore structures. FCC structures, with their high packing density and isotropic connectivity, would be particularly suited for catalysis and gas sensing, while BCC structures, characterized by lower density and anisotropic pore networks, appear advantageous for photonics and hierarchical material assembly. Therefore, precise control over the pore symmetry, connectivity, and size is essential for optimizing the performance of mesoporous materials across diverse applications. Non-equilibrium effects, particularly during solvent evaporation or other dynamic transformations, often dictate the final packing structure. A deeper understanding of these kinetic processes will enable robust control over the formation of ordered nanostructures and open new avenues for tailoring mesoporous morphologies for advanced applications. Despite the importance of achieving precise structural control, understanding the kinetics and dynamics of non-equilibrium self-assembly in an actual process, especially in a large-scale deposition process, remains challenging.

In this study, we explore precursor-assisted soft sphere close packing using BCP micelles as a model system. The BCP micelles, prepared from the widely used polystyrene-*block*-poly (ethylene oxide) (PS-*b*-PEO) in a good-poor solvent pair (one good for both PS and PEO and one selective for PEO), provide a versatile platform for studying soft sphere packing kinetics. The addition of the inorganic precursor $SnCl_4$ induces a structural transition from BCC to FCC packing, as confirmed by scanning electron microscopy (SEM) images and static grazing-incidence small-angle X-ray scattering (GISAXS) data. These findings emphasize the role of the precursor in facilitating close packing. This precursor-assisted close packing is applicable to different systems and provides a versatile platform for tailoring pore sizes of ordered mesoporous materials. To probe the kinetics of this close-packing process, in situ GISAXS during slot-die coating is carried out, complemented by dynamic light scattering (DLS) measurements. The in situ GISAXS identifies distinct kinetic regimes during the solution-to-film transition and provides mechanistic insights into the transition from disordered to closed-packed structures. The derived mesoporous SnO_2 has the advantages of medium pore size, interconnected mesopores, defect-rich surface, high specific surface area, and semiconducting properties, thus showing excellent gas sensing performances toward ethanol. By capturing the real-time progression of soft sphere packing, our study shows the underlying mechanisms governing precursor-assisted self-assembly. These kinetic insights offer a robust framework for precisely tailoring mesoporous morphologies, which will contribute to advancements in diverse technological applications beyond the demonstrated gas sensing, such as catalysis and separations.

2. Results and Discussion

2.1. Formation of Soft Spheres with Block Copolymers

BCPs undergo microphase separation and preassemble into micelles in dilute selective solvents,[26–28] serving as excellent models for investigating soft spheres. In this study, PS_{197}-*b*-PEO_{182} with a PEO volume fraction (f_{PEO}) of 0.27 is chosen and micellized in a mixture of good solvent tetrahydrofuran (THF) and PEO-selective aqueous solution (**Figure 1a**). The high ratio of THF in the solution plasticizes the PS block, reduces its glass transition temperature, and enhances the chain mobility (Figure S2, Supporting Information), facilitating the formation of equilibrium micelles.[28] With the volume ratio of 3.3 between THF and hydrochloric acid (HCl) solution, PS-*b*-PEO could form equilibrium micelles in the solution with a hydrodynamic radius of 25 nm, as determined by DLS measurements (Figure 1b and Figure S3, Supporting Information). Upon drying, the micelles become compact and feature a radius of ≈14 nm as shown in the SEM image (Figure 1c), which corresponds to a core radius of ≈12.6 nm. The BCP micelles are subsequently used as the structure templates. After introducing the inorganic precursor $SnCl_4$, this inorganic species selectively interacts with the PEO corona, coassembling with the micelles as sketched in Figure 1a. The

M. Schwartzkopf, S. Koyiloth Vayalil, S. V. Roth
Deutsches Elektronen-Synchrotron DESY
Notkestr. 85, 22607 Hamburg, Germany
S. Koyiloth Vayalil
Applied Sciences Cluster
University of Petroleum and Energy Studies UPES
Dehradun, Uttarakhand 248007, India
S. V. Roth
Department of Fibre and Polymer Technology
KTH Royal Institute of Technology
Teknikringen 56-58, Stockholm 100 44, Sweden

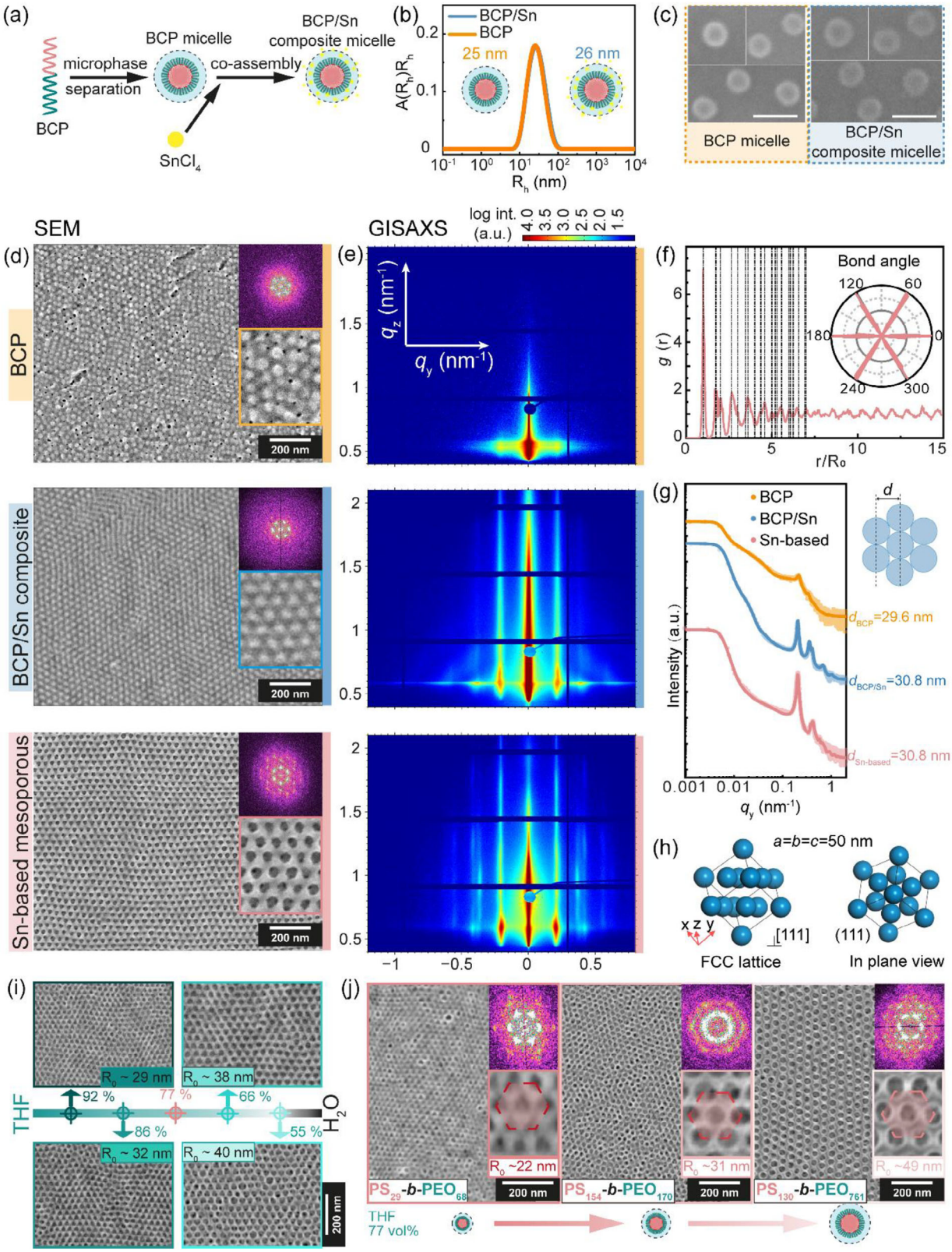

Figure 1. a) Scheme of micellization of BCP and inorganic species coassembly with BCP micelles. b) DLS results of pure BCP micelles and the mixture of BCP micelles and inorganic precursor $SnCl_4$. c) SEM images of dry BCP micelles and BCP/Sn composite micelles; the scale bars are set to 50 nm. Morphological information of pure BCP, BCP/Sn composite, and mesoporous inorganic Sn-based film with d) the left column of SEM images and e) the right column of 2D GISAXS data; the first, second, and third rows are the data of pure BCP, BCP/Sn composite, and mesoporous inorganic Sn-based

introduction of precursor leads to a slight swelling of the micelles, with the hydrodynamic radius increasing to 26 nm (Figure 1b) and a dry micelle size of ≈17 nm (Figure 1c). The increase in the size of the dry BCP/Sn composite micelles is attributed to the skin layer formed by the inorganic precursors, which prevents the complete removal of solvent from the micelles and thus contributes to their overall larger size. These observations confirm the formation of soft spheres of the BCP in solution. In the following sections, the wording soft spheres is used as an analog for BCP micelles.

2.2. Key Role of Precursor toward Close Packing

The deposition of the pure BCP solution results in an ordered sphere packing with a BCC structure, as shown in SEM images and the corresponding 2D fast Fourier transformation (FFT) patterns (Figure 1d). The absence of higher-order scattering peaks in the 2D GISAXS data (Figure 1e) indicates a limited ordering of the pure BCP film. The SEM and 2D GISAXS data suggest the loose packing of the soft spheres in the pure BCP film. However, the situation changes after the addition of the inorganic precursor $SnCl_4$. The addition of the inorganic precursor $SnCl_4$ plays a critical role in a soft sphere close packing. The BCP/Sn composite film shows a hexagonal packing with long-range order, as evidenced by SEM images and 2D GISAXS data (Figure 1d,e). The hexagonal-lattice-like structure produces distinct diffraction spots in the 2D FFT pattern and 2D GISAXS data. After removing the soft sphere template via oxygen plasma treatment, the resultant mesoporous Sn-based film retains the hexagonal-packing structure, as shown in SEM and 2D GISAXS data (Figure 1d,e). The low-magnification SEM (Figure S4, Supporting Information) reveals large packing domains (≈1 µm), which display Moiré fringes arising from the interference between sample periodic structures and SEM scanning lines.[29–31]

The in-plane structures are analyzed in detail by combining reciprocal space analysis of the SEM images with modeling of horizontal line cuts from the 2D GISAXS data. Reciprocal space analysis of the SEM image (Figure 1f) confirms the formation of a hexagonal lattice with a center-to-center distance of 35.5 nm. Due to the close-packing arrangement, the pore size of the ordered mesoporous materials is typically defined by the center-to-center distance. The pair distribution function peak positions closely match the theoretical values of the hexagonal lattice, and the bond angle analysis shows a characteristic 60° bond angle, which is consistent with the hexagonal symmetry. Horizontal line cuts from the 2D GISAXS data are stacked and modeled with the distorted wave Born approximation and local monodisperse approximation(Figure 1g). According to the results of the modeling, the pure BCP film adopts a BCC packing structure with a *d*-spacing of 29.6 nm, while the BCP/Sn composite and mesoporous Sn-based films feature a hexagonal superlattice with a slightly larger *d*-spacing of 30.8 nm. The slight shift on the second and third scattering peaks of the mesoporous Sn-based film is due to the enhanced surface details and slight surface modifications induced by oxygen plasma treatment, which does not affect the analysis results (Section S5, Supporting Information). Thus, SEM analysis and GISAXS modeling confirm the hexagonal order of these films. To extract the 3D packing structure, further GISAXS indexing is carried out with MATLAB-based software SunBIM.[32] The indexing analysis indicates an FCC packing featuring lattice parameters of $a = b = c = 50$ nm, oriented with the [111] perpendicular to the substrate (Figure 1h) in the mesoporous Sn-based film (Figure S6, Supporting Information). These results demonstrate that the incorporation of $SnCl_4$ induces a structural transformation in the soft sphere packing, promoting the formation of FCC superlattices.

2.3. Versatility of Precursor-Assisted Close Packing

The precursor-assisted close packing strategy is applicable to different systems and provides a versatile platform for fabricating mesoporous materials with tunable pore size, extending beyond the specific formulations previously discussed.

One of its key advantages lies in the ability to regulate soft sphere size by simply varying the ratio of good to poor solvents. Larger soft spheres, consequently larger pore sizes in the resulting ordered mesoporous materials, are obtained with lower volume of THF, and vice versa. To demonstrate this tunability, with a fixed HCl solution volume of 0.42 mL, decreasing volume fractions of THF from 92% to 55% leads to a corresponding increase in pore size from 29 to 40 nm, as shown in Figure 1i. This tunability arises from changes in solvent selectivity. Reducing volume fractions of THF increases the selectivity of the solvent mixture and the incompatibility between the PS core and the solvent environment, resulting in increased interaction parameter (χ) and interfacial tension.[28] These effects favor the formation of larger soft spheres with higher aggregation numbers[28] and thus larger pore sizes. This solvent-based modulation enables a tunable window of around 10 nm for PS_{197}-*b*-PEO_{182}. However, the THF volume fraction is limited by micellization at the upper end and by BCP solubility and spherical micelle stability at the lower end (Figure S7, Supporting Information).

Another approach towards tunable pore size involves tailoring the molecular weight of BCPs. As a demonstration, three PS-*b*-PEO BCPs with different molecular weights and block ratios (Table S1, Supporting Information) are used to fabricate ordered

film, respectively. f) The pair distribution function analysis of the SEM image of mesoporous Sn-based film in (d) with its corresponding bond angle plot as an inset. The x-axis is normalized to the center-to-center distance R_0, which is 35.5 nm. The black dashed lines indicate the theoretical peak positions of the 2D hexagonal lattice. g) Horizontal line cuts from 2D GISAXS data in (e) in a log–log style with the data shown as colored circles and their modeling shown as solid lines. The line cuts are shifted vertically for comparison. The top right corner inset shows the sketch of the *d*-spacing in the hexagonal packing. The *d* of different films is labeled on the right of the corresponding 1D scattering profiles. h) Sketch of FCC lattice structure with the [111] vector normal to the substrate ((111) plane parallel to the substrate). By indexing the 2D GISAXS data, the crystal unit parameters are determined to be $a = b = c = 50$ nm. Tunable pore size achieved by i) changing the volume fraction of THF in the solvent while fixing the volume of HCl solution at 0.42 mL and j) utilizing different molecular weights of PS-*b*-PEO. The volume fractions of THF decrease from 92 vol% (top left) to 55 vol% (bottom right) in (i), corresponding to the pore sizes of 29 to 40 nm. For different PS-*b*-PEO, the THF fraction is kept at 77 vol%. The pore sizes are around 22, 31, and 49 nm with BCPs of small, medium, and large molecular weight, respectively.

mesoporous materials with pore sizes ranging from 20 to 50 nm (Figure 1j). The regulating window largely covers the mesoporous range. With further optimization of molecular weights, block ratios, and solvent systems, this tuning window is expected to span almost the entire mesoporous regime and can even extend into the macroporous range. This precursor-assisted close packing is versatile and provides a robust platform for mesoporous materials with tunable pore sizes.

PS_{197}-*b*-PEO_{182} with a medium molecular weight (28500 g mol^{-1}) and a large PS block (f_{PS} 0.73) gives medium-sized pores, which balances the pore density, mechanical stability, pore size, and specific surface area. The relatively large PS block ensures micelle formation, which is then kinetically trapped in the early stages for in situ studies of soft crystallization. Therefore, PS_{197}-*b*-PEO_{182} is chosen for the *in-situ* study and further gas sensing applications. Due to the versatility of the precursor-assisted close packing, this system serves as a representative model to provide general insights into soft crystallization processes.

2.4. Kinetical Insights into Closing Packing

2.4.1. Time-Resolved Soft Crystallization

The self-assembly process is monitored using in situ GISAXS measurements, providing insights into the temporal evolution of structural ordering (**Figure 2**a). Figure 2b,c shows the evolution of the relative mass and thickness of the film, respectively. The 1D in-plane GISAXS curves are obtained by performing horizontal line cuts at the Yoneda band (marked with a yellow dashed rectangle in Figure 2a) of the film, and 1D out-of-plane GISAXS curves are obtained by performing vertical line cuts on the first-order scattering signals (marked with a red dashed rectangle in Figure 2a) in the 2D GISAXS data. The qualitative analysis of GISAXS data is presented in Section S8B, Supporting Information. Figure 2d,e shows the temporal evolution of out-of-plane and in-plane scattering signals, respectively. After deposition, the relative mass and thickness both undergo an exponential decay. Based on the results of Figure 2, the self-assembly process can be divided into six distinct stages: dilute dispersion (stage I: 0–40 s), concentrated dispersion (stage II: 40–60 s), wet film (stage III: 60–170 s), structuring wet film (stage IV: 170–280 s), gel film (stage V: 280–370 s), and glassy film (stage VI: >370 s) states.

During the initial dilute dispersion stage, the dispersion undergoes rapid changes in relative mass and thickness. After 40 s, about 70% of the mass evaporates, which is attributed to the evaporation of the volatile solvent THF. These changes in relative mass and thickness dramatically increase the concentration of soft spheres and transitions the solvent quality from slightly PEO-selective to highly PEO-selective. The resulting high χN condition freezes chain exchange between micelles, thereby effectively trapping the dynamics of soft spheres (Figure S9, Supporting Information).[33–35] In this dilute solution stage, micelles exist as discrete spheres with little interaction, gradually shrinking in size due to the deswelling (Figure S10, Supporting Information). Limited scattering signals are observed in both out-of-plane (q_z) and in-plane (q_y) directions, except for the strong scattering at q_y = 0 nm^{-1} as shown in 2D GISAXS data at 30 s (Figure 2g). Following rapid solvent evaporation, the dispersion enters the concentrated dispersion stage. During this concentrated dispersion period, the critical concentration and thickness of the dispersion are achieved, leading to rapid signal development in both q_z and q_y directions (Figure 2d,e). At the end of this rapid development, the dispersion is transitioned into film stages.

During the wet film stage, the remaining solvent is mainly an HCl/H_2O azeotrope (20.2 wt% HCl solution), and this wet film features a dense fluid phase of soft spheres. The increased concentration and viscosity slow down changes in mass and thickness (Figure 2b,c). As the inter-distances of soft spheres decrease to a scale comparable to their sizes, interactions between soft spheres come into play. This is evidenced by broad scattering lobes in the in-plane scattering profiles, as exampled by a white rectangle in the 2D GISAXS data at 120 s (Figure 2g). At the same time, packing clusters of soft spheres are identified by weak diffraction peaks, as highlighted with yellow rectangles in Figure 2e,f. The *d*-spacing of these packing clusters decreases over time, as indicated by the slight peak shifts in their q_y positions to higher values. Two distinct Yoneda bands are visible in the 2D GISAXS data at 120 s (Figure 2g): one at the higher q_z position originating from the Si substrate and another at a lower q_z position resulting from the soft sphere composites. The Yoneda band from the micelle composites shifts to higher q_z values during drying, as highlighted with red rectangles in Figure 2d,f, reflecting condensation and an increase in the average electron density of the soft sphere composites as the solvent is evaporating.

As the film transitions into the structuring wet film state, both relative mass and thickness stabilize (Figure 2b,c). The ring-like signal in the 2D GISAXS data (highlighted by a white dashed curve in Figure 2g at 210s) refers to the contribution of the form factor of soft spheres (Section S11, Supporting Information). During this structuring wet film state, the packing of soft spheres is developing with Bragg peaks appearing in the q_y and q_z directions (Figure 2d,e). Indeed, an in-plane packing of soft spheres is preferred during this structuring wet film state since the high-order Bragg peaks in the q_y direction appear earlier than those in the q_z direction.

In the gel film state, the film solidifies with largely fixed structures. Both mass and thickness show little changes (Figure 2b,c), and the scattering peaks in the in-plane GISAXS curves stabilize. However, the Bragg peaks in the q_z direction transform into oscillations, signaling the development of out-of-plane packing domains. The signal feature of 2D GISAXS data stabilizes after 370 s (Figure 2g) with a fully developed scattering pattern, which is in perfect accordance with the ex situ GISAXS data and, therefore, the signal of the final state, reflecting the final stage in the kinetic process. The formed nanostructures are solidified and preserved as most solvents are removed. Thus, the polymer film throughout the course of stage VI is in its glassy film state.

To gain deeper insights into the morphology evolution, horizontal line cuts with a time increment of 20 s are selected (**Figure 3**a). A detailed examination of the GISAXS data is presented in Figure 3b–f. Figure 3b displays the integrated intensity (intg. intensity) of horizontal (q_y) and vertical (q_z) line cuts. The critical angles of the BCP composite film are extracted from their vertical cuts and plotted versus time as in Figure 3c, providing the temporal evolution of the average density of the composite film. From the modeling of the horizontal line cuts, the

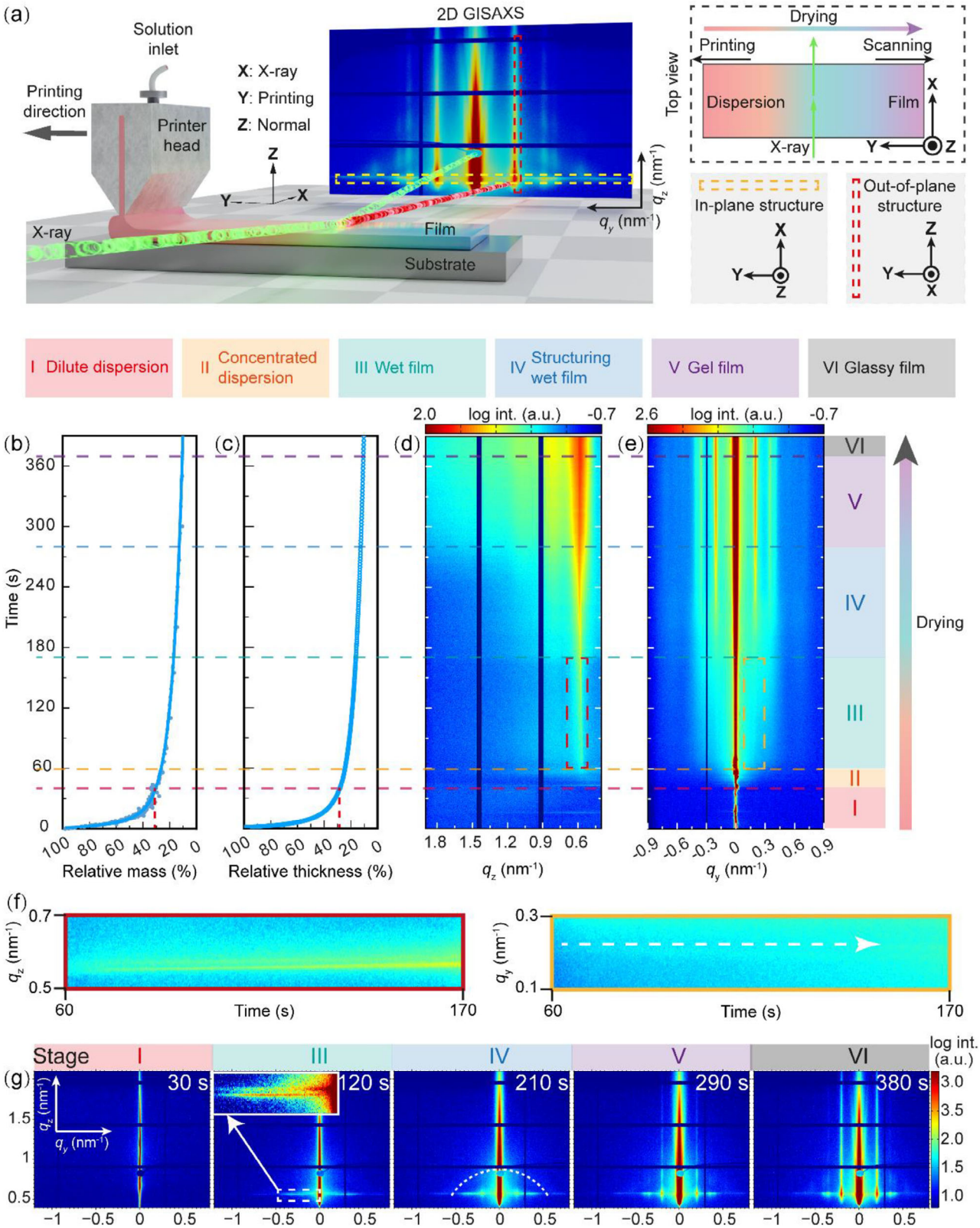

Figure 2. a) Schematic of the in situ GISAXS setup with 3D coordinate system. The x, y, and z directions align with the X-ray, printing direction, and substrate normal, respectively. The yellow and red rectangles in the 2D detector pattern indicate the horizontal and vertical line cuts, which encode the information about in-plane and out-of-plane structures, as shown in the bottom right corner. The top right corner shows the top view of the in situ measurements with measurement scanning in the opposite direction of the printing direction. The temporal evolution of b) relative mass and c) relative

radius (R) and center-to-center distance (D) of the micelles are obtained. The R and D of different packings are shown here, as illustrated in Figure 3d. The full width at half maximum (FWHM) obtained from modeling is used to derive the domain size with the Scherrer equation, as shown in Figure 3e. To further investigate the progression toward close packing, Lorentzian fits of the first Bragg peak ($q_y \approx 0.2$ nm^{-1}) are performed, yielding the integrated area (intg. area), which is presented in Figure 3f. These metrics offer quantitative insights into the packing order and structural evolution. Additional details of the scattering data analysis are provided in Section S8, Supporting Information.

2.4.2. Kinetically Trapped Micelles in Dispersion Stages

GISAXS data reveal little structural information in the dilute dispersion stage due to the limited scattering features and signals. During this dilute dispersion stage, soft spheres exist as discrete spheres with negligible interactions. As volatile solvent THF evaporates, the system gradually shifts to highly PEO-selective, driven away from its equilibrium state. This shift in the solvent environment may trigger micelle dynamic changes, such as single-chain exchange and micelle fusion/fission, leading to changes in micelle size and structure.

The chain exchange rates are extremely slow in corona-selective solvents[33,36] and, for example, slow down by 5 orders of magnitude when adding only 25 vol% corona-selective solvents to the system.[34,35] As shown in Figure S9 (Supporting Information), chain exchange becomes virtually prohibited once the evaporation process starts. Regarding fusion/fission, the emergence of a new micelle population with larger sizes, as well as a bimodal distribution, is expected. However, during evaporation, all autocorrelation functions of DLS measurements show single decay (Figure S11, Supporting Information), indicating single-size distributions of the soft spheres and no apparent fusion or fission. This finding suggests that the soft spheres are actually kinetically trapped during the evaporation of volatile solvents.[28,36] As a result, the micelles maintain their spherical shape while gradually shrinking in hydrodynamic size from 52 to ≈35 nm (Figure S10, Supporting Information) due to the compaction of spheres. The scattering signal from these kinetically trapped micelles is further attenuated by the surrounding liquid medium. Consequently, during the first 40 seconds of evaporation, the intg. intensity in both the q_y and q_z directions remains weak and stable.

After the dilute dispersion stage, about 70% of the mass is lost, resulting in concentration dispersion. Between 40 and 60 s, a transition window is observed in this concentrated dispersion stage, which features a dramatic intensity increase (Figure 3b). This transition corresponds to the period of achieving a critical concentration and thickness of the liquid film and was observed in other systems before.[26,27] Significant scattering signals and features are appearing in the q_y direction (Figure S13, Supporting Information) in this transition period.

2.4.3. Dense Fluid Phase in Wet Film Stage

Once the rapid transition in concentrated dispersion stage completes, the dispersion changes into film stages, starting with the wet film stage, which features a dense fluid phase of soft spheres.

In this wet film stage, changes in scattering intensity and features slow down but still evolve, as seen in the horizontal line cuts between 60–180 s (Figure 3a and Figure S14, Supporting Information) and the intg. intensity (Figure 3b). The increased intensity along q_y arises from multiple contributions as shown in Section S8B, Supporting Information. The scattering contrast and number density of scattering objects increase, as evidenced by the continuous shifting in the critical angle of the BCP composite film (Figure 3c). During this wet film stage, the soft spheres maintain a stable size, with a compacted PS core and a swollen PEO corona dispersed in the aqueous solution. As the inter-distance between the spheres decreases to the point where it becomes comparable to the sizes of the spheres, interactions between the spheres start to play a role. In-plane spheres with a broad inter-distance distribution can be observed (Figure 3d), featured by broad scattering lobes in the range of 0.1–0.5 nm^{-1} in the horizontal line cuts (Figure 3a and Figure S14, Supporting Information).[37]

Weak diffraction peaks within the broad peak (Figure 2f) indicate the formation of well-defined packing clusters, most likely in a hexagonal structure. These clusters may exist in the bulk of the liquid film or at the film/substrate and film/air interfaces. If these packing clusters were located at the film/substrate interface or within the bulk, their scattering intensity would be expected to increase due to the less attenuated signal during film drying and thinning. However, the relatively stable intensity observed in the wet film stage suggests that the localization is at the film surface rather than at the film/substrate interface or within the film bulk. This phenomenon aligns well with previous knowledge that concentration gradients of solute in films exist during the solvent evaporation.[38–40] At the surface, where the concentration of soft sphere is high, these crowded soft spheres tend to pack into 2D hexagonal clusters. Similar hexagonal packing at liquid surfaces was reported for various systems before,[41–43] and these clusters could serve as nucleation seeds during the following crystallization process. However, no packing or obvious structures are observed in the out-of-plane direction, as evidenced by the relatively stable intg. intensity along the q_z direction (Figure 3b). This

thickness. The mass changes are obtained by a balance, and the relative thickness is calculated based on mass changes. 2D contour mappings of the d) vertical and e) horizontal line cuts extracted from 2D GISAXS data. All vertical line cuts are integrated at a constant q_y value of the first Bragg peak position, and horizontal line cuts are integrated over the corresponding Yoneda region as indicated by two rectangles in (a). The x-axis is the relative mass (%), relative thickness (%), q_z (nm^{-1}), and q_y (nm^{-1}) for (b–e), respectively. The y-axis for (b–e) is time in seconds and aligned with the same scale and range for presentation. Six stages, namely I dilute dispersion, II concentrated dispersion, III wet film, IV structuring wet film, V gel film, and VI glassy film states, are observed in the film formation as separated by colored dashed lines. The red dashed rectangle in (d) highlights the evolution of the Yoneda band, and the yellow dashed rectangle in (e) highlights the presence of the Bragg peak in the wet film stage. These two highlight rectangles are zoomed in, as shown in (f). The white dashed arrow in the right panel of f) highlights the weak diffraction peaks inside broad scattering peaks. g) Selected 2D GISAXS data during film formation at different times as indicated. The white rectangle in a snapshot at 120 s highlights the two Yoneda bands, and the white dashed curve indicates the weak ring-like signal at 210 s.

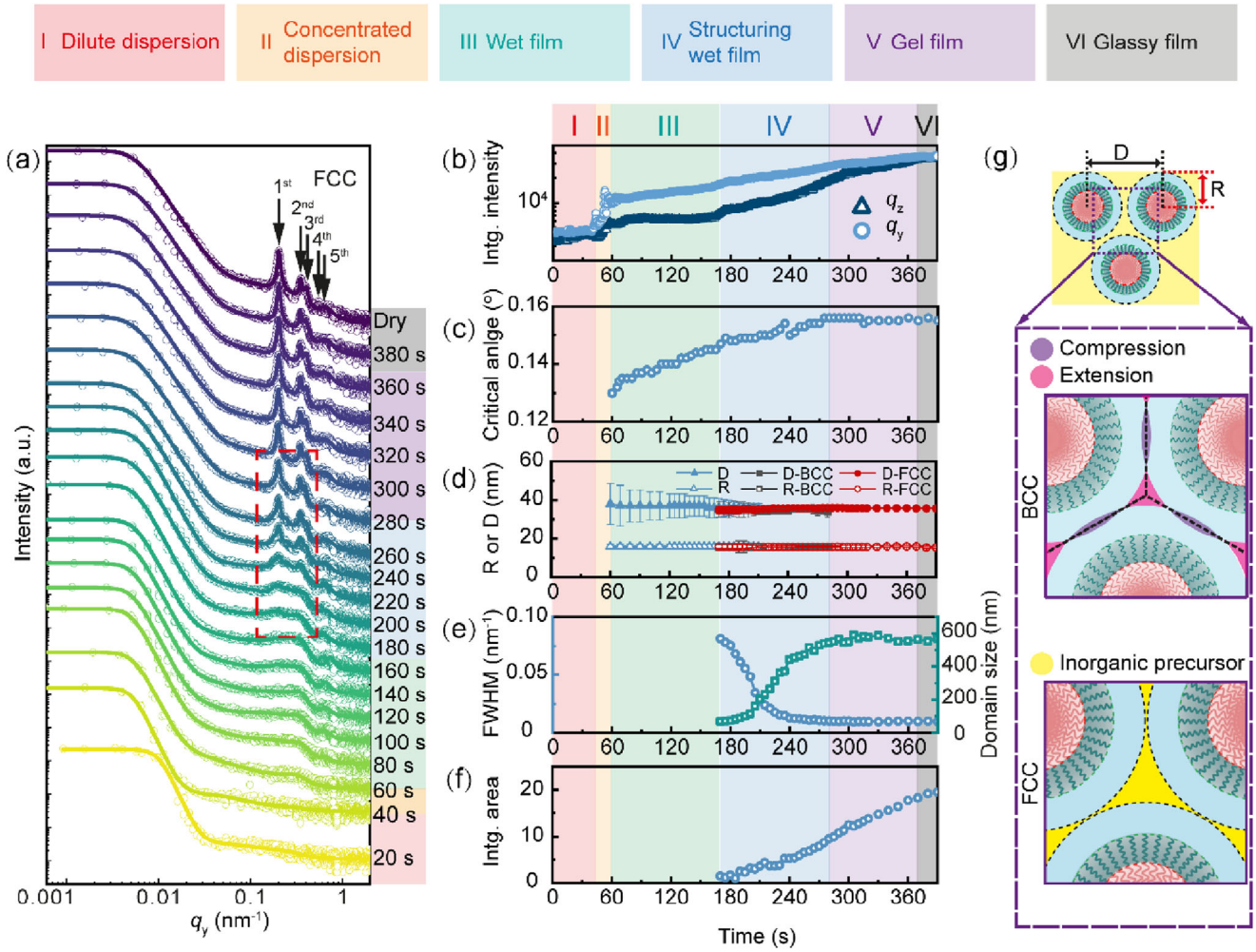

Figure 3. a) Selected horizontal line cuts of 2D GISAXS data (circles) and corresponding modeling results (lines) are stacked vertically from bottom to top. The position evolution of Bragg peaks is highlighted by the red rectangle, and the Bragg peak positions of the FCC structure are indicated by black arrows. The transition from BCC to FCC during the wet stage is highlighted by a red dashed rectangle. b) Integrated intensity (intg. intensity) evolution over time is obtained by integrating the intensity of horizontal (q_y) or vertical (q_z) line cuts. c) Evolution of critical angle over time. The critical angle of the composite film is determined by the local maximum from vertical line cuts. d) Characteristic radii (R) and center-to-center distance (D) are determined from modeling results of the horizontal line cuts. The blue triangles, black squares, and red circles represent amorphous, BCC, and FCC packings, respectively. e) Full width at half maximum (FWHM) and corresponding domain size. The corresponding domain size is determined by the Scherrer equation with a shape factor of 0.9. f) The integrated area (intg. area) evolution of the Bragg peak ($q_y = 0.2$ nm^{-1}) is obtained by Lorentzian fits. The intg. area represents the relative crystallinity of the soft sphere packing. g) Sketch of two different conditions of soft sphere interaction. The upper one shows the deformation of three soft spheres due to the corona overlapping. The boundary of the corresponding Wigner–Seitz cell is sketched with black dashed lines. The overlapping is shaded by purple and pink to show the compression or extension force in this area. The bottom one shows the FCC packing of three soft spheres without the corona overlapping. The inorganic precursors fill the voids between spheres, alleviate the packing frustration, and stabilize the close packing phases.

finding underscores the predominantly surface-localized nature of the packing clusters during this stage of the film formation process.

2.4.4. In-Plane Crystallization at Surface in Structuring Wet Film Stage

With hexagonal packing clusters and concentrated micelles, ordered structures develop rapidly at the film surface during the structuring wet film stage. In this stage, crowded soft spheres come into contact, as depicted in Figure 3g. Seeding with hexagonal nuclei, FCC packing domains develop quickly at the surface.

The formation of FCC structures, instead of BCC, in the hybrid system is primarily attributed to the presence of the inorganic precursor. Simulations and experimental studies consistently indicate that BCC packing dominates the phase diagram of soft spheres at low solvent fractions.[17–19] In the system of pure soft spheres, as the solvent evaporates, micelles are forced to come close to fill the interstitial space and tend to form FCC first and then transform into BCC structures.[17,19] This behavior is consistent with our observation in the pure BCP system

where soft spheres form a BCC structure after solvent evaporation (Figure 1d,e). As shown in Figure 1, for the pure soft sphere system, the inter-distance of soft spheres is 31.4 nm, corresponding to a measured *d*-spacing of 29.6 nm, and slightly smaller than their diameters ($2R \approx 34$ nm). This overlapping of soft spheres causes local compression and extension as sketched in the upper row of Figure 3g. However, the situation changes significantly with the addition of the inorganic precursor. The strong acidity of the solution controls the hydrolysis-condensation process of the precursor and maintains the precursor as stable nanoparticles. Additionally, the weak interaction between the precursor $SnCl_4$ and the PEO corona allows the precursor to preserve its fluidity and occupy the interstitial spaces between soft spheres (Figure 3g). During solvent evaporation, the concentrations of soft spheres and precursors significantly increase. These concentrated precursors effectively mitigate the packing frustration experienced by soft spheres by filling the far reaches of the Wigner-Seitz cells, favoring the stabilization of FCC structures over BCC. Consequently, this precursor-assisted close packing leads to a larger inter-distance *D* (Figure 3g). This "filler" effect of the precursor is analogous to the role of solvents or homopolymers in pure polymer systems, where additive components reduce packing frustration and favor the stabilization of close-packing phases.[44–47] By enabling efficient volume filling and reducing packing frustration, the precursor facilitates the formation of more stable FCC structures, highlighting its crucial influence on the assembly process.

Some non-close packings, characterized as BCC structures, are observed, which transition into FCC structures during the structuring wet film stage (Figure 3d), as highlighted by red rectangles in Figure 3a and Figure S15 (Supporting Information). This structural transition leads to a packing density increase, as BCC packing features a packing density of 0.68, while FCC packing achieves a higher density of 0.74. At the same time as the structure transformation, the domain sizes grow significantly from 40 nm to ≈600 nm, as indicated by the FWHM (Figure 3e). The intg. area also increases but in a linear behavior as shown in Figure 3f, which is driven by increased scattering contrast and overall crystallinity.

2.4.5. Out-of-Plane Crystallization in Gel Film Stage

Following rapid structure development in the structuring wet film stage, the packing structure achieves a relatively stable configuration in the gel film stage, characterized by constant values for R, D, and FWHM. The surface layer of BCP micelles is already packed into domains, resulting in stable in-plane structural parameters. However, even though domain size ceases to grow, the crystallinity of the packing structure continues to increase (Figure 3f) due to the crystallization advancing inward along the out-of-plane direction. This inward crystallization behavior has also been reported in other systems, such as colloidal systems.[48,49]

In this gel film stage, the out-of-plane crystallization progression is evidenced by the increasing intg. intensity of both q_y and q_z (Figure 3b) and the emerging Bragg peaks in q_z direction (Figure 2d). The high concentration of soft spheres and precursors results in a high viscosity and a negligible evaporation rate, leading to minimal changes in the relative mass, thickness, and critical angle.[27,50] However, the soft spheres still retain a degree of mobility in the gel stage, allowing them to adjust their positions to minimize overall free energy. Soft spheres in the bulk region attach to the surface-packing layer and grow epitaxially in the out-of-plane direction, extending the crystallization from the surface toward the substrate. This bulk order enhances in-plane crystallinity without obviously affecting the FWHM of in-plane structures. The increased coherence along the out-of-plane direction results in pronounced Bragg peaks in the q_z direction, as indicated by Figure 2d,g. This residual solvent-assisted crystallization process is similar to the effects of solvent vapor annealing, which is a widely used technique for improving ordering in BCP thin films.[51–53] The presence of a corona-selective solvent enhances micelle mobility, which further optimizes the packing lattice and increases overall crystallinity.

In this gel film stage, the out-of-plane growth introduces relief terraces. Achieving perfect close-packing is often hindered by mismatches between the number of soft spheres and the requirements for perfect close-packing arrangements. As the film dries, these mismatches undulate in thickness to reconcile the commensurability between film thickness and inter-domain spacing, thus resulting in surface relief terraces. These surface relief terraces often appear in lamellae-, cylinder-, and sphere-forming BCP thin films with islands, holes, or bicontinuous relief microstructures.[54] This terrace topology produces tilted strike signals in the 2D GISAXS data (Figure 2g and Figure S16, Supporting Information).[55] As the film dries, the relief terraces on the film surface become increasingly pronounced (Figure S16, Supporting Information). Such surface undulation has been widely observed in polymer films.[37,56]

At the end of the gel film stage, all structures are developed and fixed. The formed nanostructures are solidified and preserved as most solvents are removed from the film. Thus, the polymer film throughout the course of stage VI is in its glassy film state. The 2D GISAXS data (Figure 2g) stabilize after 370 s with a fully developed scattering pattern, which is in perfect accordance with the ex situ GISAXS data and therefore the scattering signal characterizing the final stage.

2.5. Soft Crystallization Pathway

The soft crystallization pathway of soft spheres, schematically illustrated in **Figure 4**, undergoes six distinct stages driven by solvent evaporation, micelle interactions, and precursor effects and ultimately yields an FCC packing structure.

In the initial dilute dispersion stage, PS-*b*-PEO undergoes microphase separation in the good-poor solvent pair (THF-HCl solution) and forms discrete soft spheres. As the volatile solvent THF evaporates, the size of the soft spheres shrinks and eventually stabilizes in an aqueous environment. These micelles are kinetically trapped and lack interactions in the dilute solution. After the majority of THF evaporated, the film transitions into a concentrated dispersion stage, which is characterized by a rapid increase in scattering intensity due to achieve critical concentration and film thickness.

Following the transition stage, the dispersion changes into the film. The wet film stage features a dense fluid with an increased

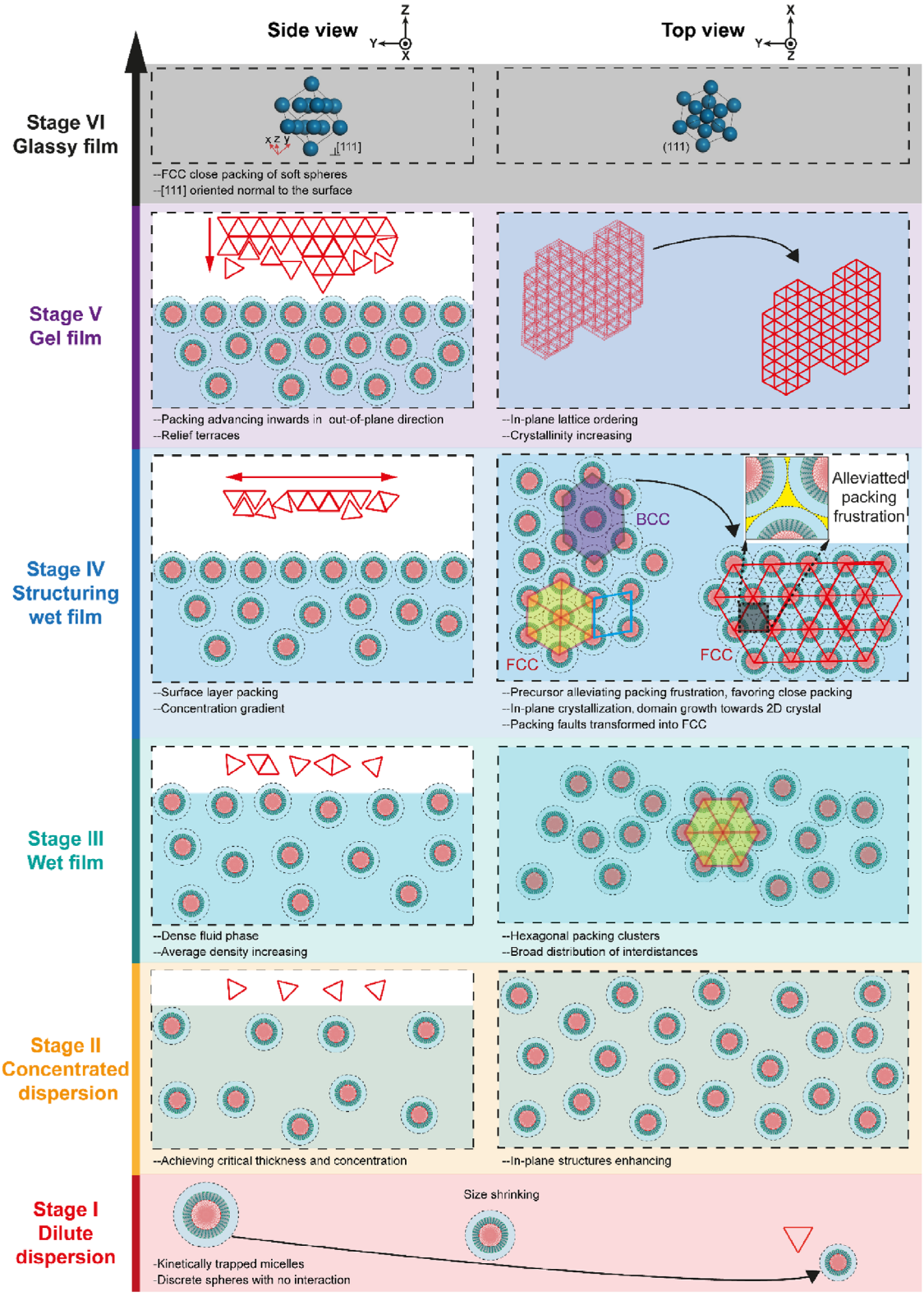

Figure 4. Sketch of proposed pathways for soft sphere close packing. Stages I, II, III, IV, V, and VI represent dilute dispersion, concentrated dispersion, wet film, structuring wet film, gel film, and glassy film, respectively, as shown in the left column with different colors. The middle column provides a side view, depicting the evolution of the out-of-plane structure during soft crystallization, while the right column presents a top view, indicating the in-plane structural transformations at each stage. The bullet points under each sketch highlight the features of different stages. Stage I is a dilute solution in which the side view and top view both show discrete spheres with shrinking sizes.

viscosity and sphere concentration as well as a decreased evaporation rate. In this stage, the inter-sphere distance decreases to values comparable to the sizes of soft spheres, consequently forming a dense fluid phase. In this dense fluid phase, the interactions between the crowded spheres come to play, leading to a broad distribution of inter-sphere distances and the formation of surface packing clusters. These hexagonal clusters at the surface serve as nuclei for subsequent in-plane crystallization.

With the packing clusters at the surface, the structuring wet film stage witnesses a rapid structure development in the in-plane direction. This in-plane crystallization is driven by the packing of soft spheres at the film surface, where precursors in the voids between soft spheres mitigate packing frustration and thus stabilize the close packing. Non-close packings, such as BCC structure, transform into a hexagonal packing. During this stage, the domain size grows from 40 nm to ≈600 nm with the decreasing FWHM of the Bragg peak. This surface packing serves as nuclei for subsequent inward crystallization in the gel film stage.

In the gel film stage, the evaporation rate slows down to a negligible level. Although the surface structure is largely fixed, the soft spheres in the bulk retain mobility, allowing their attachment to the surface packing layer. This results in out-of-plane crystallization, with ordering advancing inward from the surface to the substrate. Out-of-plane growth introduces surface relief terraces. Thickness undulations arise from the mismatch between film thickness and inter-domain spacing, and these undulations and terraces evolve more pronouncedly during the structuring wet film and gel film stages. At the end of the gel film stage, the soft spheres packing stabilizes into an FCC arrangement with high crystallinity. The precursor's role in filling interstitial voids proves essential, as it alleviates packing frustration and favors the stability of the FCC structure. The resulting film exhibits a well-ordered, close-packed mesostructure.

2.6. Ordered Mesoporous SnO_2 for Gas Sensing

The pure BCP and BCP/Sn composite are compact films without semiconducting properties, whereas the close-packing mesoporous materials derived from BCP/Sn composite inherently possess high specific surface areas and an interconnected pore network, making them a promising candidate for gas sensing applications. To achieve high crystallinity without mesostructure destruction, a well-established two-step sequential calcination process, the calcination in inert N_2 followed by air, is selected to obtain crystalline mesoporous materials from the BCP/Sn composites.[57–59] X-ray diffraction (XRD) analysis (**Figure 5a**) confirms the formation of crystalline rutile-type SnO_2 with a tetragonal $P4_2/mnm$ symmetry and a crystallite size of 2.7 nm. UV–Vis spectroscopy (Figure 5b) indicates a direct bandgap of 3.86 eV, which is blue-shifted from the bulk value (3.60 eV) due to structural defects and nanoscale size effects, in agreement with previous reports and the effective mass approximation.[60] Photoluminescence (PL) spectroscopy and its deconvolution (Figure 5c) show strong emission peaks in both the UV and visible regions, mainly arising from oxygen vacancies and related intrinsic defects.[60–63] This defect-rich nature is also confirmed by Raman spectroscopy as shown in the inset of Figure 5c. The intense 574 and 235 cm^{-1} modes arise from in-plane oxygen defects and subbridging and bridging oxygen defects, respectively.[64] These defect-rich nanocrystallites are promising for gas sensing due to the positive correlation between defect density and active site availability. While SnO_2 has been widely used in gas sensors, conventional thick films often lack sensitivity at low analyte concentrations.[62] The development of ordered mesoporous SnO_2, as demonstrated here, offers a compelling strategy to improve detection performance.

The gas sensing process mainly relies on diffusion, adsorption, and a surface reaction between the target gas and adsorbed oxygen species on the active materials (Figure 5d).[58,59,65] SnO_2, a typical n-type semiconductor, features electrons as charge carriers. The adsorbed oxygen molecules on SnO_2 could be activated as O_x^- species, such as O_2^-, O^-, and O_2^-, by extracting electrons from the conduction band, resulting in the formation of an electron depletion layer near the surface and thus an increase in electrical resistance.[62,66] Upon exposure to reducing gases like ethanol, the adsorbed oxygen species on SnO_2 react with these gases (ethanol + O_x^- = CO_2 + H_2O + e^-), releasing the trapped electrons back to the conduction band and leading to a decreased resistance in sensors.

Owing to the medium pore size, interconnected mesopores, defect-rich surface, and high specific surface area (Figure 5d), ordered mesoporous SnO_2 facilitates efficient gas diffusion, adsorption, and interaction. The mesoporous SnO_2-based gas sensor shows excellent response and reversibility, with response values ranging from 3 to 58 over an ethanol concentration range of 1–25 ppm, showing a good linear relationship at 250 °C (Figure 5e–g). Upon exposure to 5 ppm ethanol, the ordered mesoporous SnO_2 sensor shows a higher response value (12.3), and fast response /recovery dynamics (12/75 s, Figure 5h). Based on the well-established calculation approach,[67,68] the limit of detection for the mesoporous SnO_2 sensor is calculated to be 18 ppb, showing a great potential for the detection of trace ethanol. By contrast, commercial SnO_2 nanoparticles, with a particle size of 50 nm, a similar crystallite size of 2.6 nm, and the same rutile-type crystal structures as the mesoporous SnO_2,[69] are deliberately chosen and used to construct a reference sensor, which exhibits a significantly lower response value (8.5) and longer response time (49 s) toward 5 ppm ethanol under the same test conditions (Figure 5i). To ensure the accuracy of the comparison, both sensors are tested simultaneously in the same chamber, with the exact same start times for response and recovery. The enhanced performance of the ordered mesoporous SnO_2 sensor is attributed to its defect-rich surface, as evidenced by UV–vis and PL spectroscopy, and its high specific surface area, which together increase the density of gas-sensitive active sites and contribute to a stronger sensing signal (Figure 5h,i).[59,65] The faster response rate is primarily due to the efficient Knudsen diffusion of analytes inside the interconnected mesoporous channels with medium size.[59,65] Additionally, this mesoporous SnO_2 sensor displays excellent cycling stability with a well-retained response signal (Figure 5j), confirming its robust operational reliability.

3. Conclusion

In summary, this work presents a kinetic investigation into the crystallization pathway of soft spheres assisted by precursors, leading to the formation of a well-ordered FCC mesostructure.

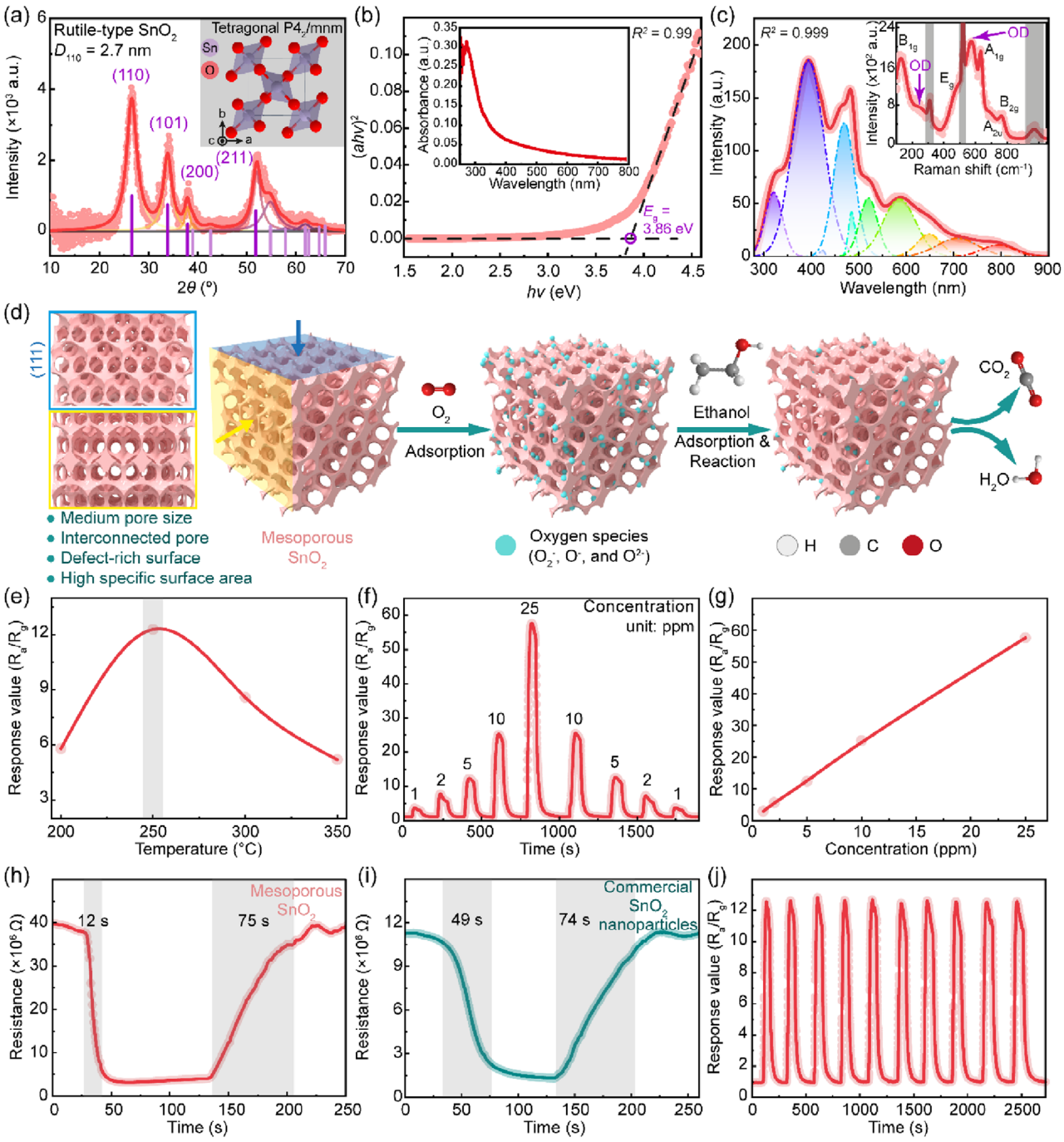

Figure 5. a) XRD spectra of the ordered mesoporous SnO_2 film after the two-step sequential calcination. The theoretical diffraction positions of rutile-type SnO_2 with a tetragonal *P*42/*mnm* symmetry are indicated with purple lines. The crystal structure is sketched in the top-right inset. The crystallite size is calculated by the Scherrer equation with a shape factor of 0.89. b) Tauc plot from UV–Vis absorption spectra with the direct allowed transition for SnO_2. Dashed lines indicate the corresponding linear fits of Tauc plots (R^2 of 0.99). The corresponding absorption spectroscopy is shown in the inset. c) Defects revealed by PL spectroscopy and Raman spectroscopy (top right inset). PL spectroscopy is recorded in the range of 280–900 nm; the deconvolution of the PL spectra is conducted with Gaussian fits (R^2 of 0.999). The top right inset shows the Raman spectroscopy. The signal from the Si substrate is shaded by gray rectangles. Different Raman modes of SnO_2 are labeled, and oxygen defects (OD) are highlighted in purple. d) Schematic illustration of the reaction on the surface of the mesoporous SnO_2. e) Responses of the mesoporous SnO_2 sensor to 5 ppm ethanol at a temperature range of 200–350 °C. Response value is defined as the ratio of the sensor resistance in air (R_a) to resistance in tested gas (R_g) for reducing gases ($S = R_a/R_g$). f) Response–recovery curve of the mesoporous SnO_2 sensor under different ethanol concentrations at 250 °C. g) Response of the mesoporous sensor versus ethanol concentrations at 250 °C. Response-recovery curve of sensors based on h) mesoporous SnO_2 and i) commercial SnO_2 nanoparticles, with a particle size of 50 nm, a similar crystallite size of 2.6 nm, and the same rutile-type crystal structures as the mesoporous SnO_2,[69] at 250 °C. To ensure the accuracy of the comparison, both sensors are tested simultaneously in the same chamber, with the same start times for response and recovery. j) Repeating the response-recovery curve of the mesoporous SnO_2 sensor to 5 ppm ethanol at 250 °C to illustrate the cycling stability.

This precursor-assisted assembly is versatile and provides a robust platform for ordered mesoporous materials with tunable pore sizes. The derived mesoporous SnO_2 has the advantages of medium pore size, interconnected mesopores, defect-rich surface, high specific surface area, and semiconducting properties, thus showing superior gas sensing performances toward ethanol. The crystallization process shows six distinct stages, namely dilute dispersion, concentrated dispersion, wet film, structuring wet film, gel film, and glassy film states. It is driven by solvent evaporation, micelle interactions, and the critical role of the inorganic precursor.

Initially, discrete soft spheres form via BCP microphase separation in a good-poor solvent mixture, which are kinetically trapped with few interactions. As solvents evaporate, the soft spheres stabilize in an aqueous environment. Transitioned from concentrated dispersion state, the film turns into wet film, where high micelle concentration and reduced inter-sphere distance lead to interactions and the formation of surface packing clusters. These packing clusters act as nucleation sites, initiating a rapid in-plane crystallization in the following structuring wet film stage. Precursors occupying voids between micelles mitigate packing frustration, promoting the formation of FCC packing with significant domain growth. In the gel film stage, out-of-plane crystallization occurs as soft spheres in the bulk attach to the surface lattice, advancing order inward. This epitaxial growth increases crystallinity and introduces surface undulations due to thickness mismatch. Ultimately, the film stabilizes into an FCC-packed structure in the glassy film stage.

This work highlights the intricate interplay of solvent dynamics, micelle interactions, and precursor effects, providing valuable insights into the precise design and fabrication of nanostructured materials, which will contribute to advancements in diverse technological applications beyond the demonstrated gas sensing, such as catalysis and separations.

Supporting Information

Supporting Information is available from the Wiley Online Library or from the author.

Acknowledgements

This work was supported by funding from the Deutsche Forschungsgemeinschaft (DFG, German Research Foundation) by Germany's Excellence Strategy–EXC 2089/1-390776260 (e-conversion), TUM.solar in the context of the Bavarian Collaborative Research Project Solar Technologies Go Hybrid (SolTech), the Center for NanoScience (CeNS) and the International Research Training Group 2022 Alberta/Technical University of Munich International Graduate School for Environmentally Responsible Functional Hybrid Materials (ATUMS), the NSF of China (Grant No. 22125501, U22A20152), and China Postdoctoral Science Foundation (Grant No. 2024M760507). G.P., L.L., and J.Z. acknowledge the financial support from the China Scholarship Council (CSC). The authors acknowledge DESY (Hamburg, Germany), a member of the Helmholtz Association HGF, for the provision of experimental facilities. Parts of this research were carried out at PETRA III. Data was collected using beamline P03 operated by DESY Photon Science. The authors thank Prof. Alexander Holleitner and Peter Weiser for providing access to the SEM. This work benefited from the use of the SasView application, originally developed under NSF award DMR-0520547. SasView contains code developed with funding from the European Union's Horizon 2020 research and innovation program under the SINE2020 project, grant agreement No 654000.

Open access funding enabled and organized by Projekt DEAL.

Conflict of Interest

The authors declare no conflict of interest.

Data Availability Statement

The data that support the findings of this study are available from the following public repository: https://doi.org/10.14459/2025mp1793803.

Keywords

block copolymer, close packing, in situ grazing-incidence small-angle X-ray scattering, kinetics, soft crystallization

Received: March 6, 2025
Revised: August 15, 2025
Published online:

[1] M. R. Begley, D. S. Gianola, T. R. Ray, *Science* **2019**, *364*, aav4299.
[2] V. N. Manoharan, *Science* **2015**, *349*, 1253751.
[3] Q. F. He, J. G. Wang, H. A. Chen, Z. Y. Ding, Z. Q. Zhou, L. H. Xiong, J. H. Luan, J. M. Pelletier, J. C. Qiao, Q. Wang, L. L. Fan, Y. Ren, Q. S. Zeng, C. T. Liu, C. W. Pao, D. J. Srolovitz, Y. Yang, *Nature* **2022**, *602*, 251.
[4] R. Montis, L. Fusaro, A. Falqui, M. B. Hursthouse, N. Tumanov, S. J. Coles, T. L. Threlfall, P. N. Horton, R. Sougrat, A. Lafontaine, G. Coquerel, A. D. Rae, *Nature* **2021**, *590*, 275.
[5] K. Zhu, S. Pazos, F. Aguirre, Y. Shen, Y. Yuan, W. Zheng, O. Alharbi, M. A. Villena, B. Fang, X. Li, A. Milozzi, M. Farronato, M. Muñoz-Rojo, T. Wang, R. Li, H. Fariborzi, J. B. Roldan, G. Benstetter, X. Zhang, H. N. Alshareef, T. Grasser, H. Wu, D. Ielmini, M. Lanza, *Nature* **2023**, *618*, 57.
[6] K. J. Si, Y. Chen, Q. Shi, W. Cheng, *Adv. Sci.* **2018**, *5*, 1700179.
[7] C. L. Bassani, G. van Anders, U. Banin, D. Baranov, Q. Chen, M. Dijkstra, M. S. Dimitriyev, E. Efrati, J. Faraudo, O. Gang, N. Gaston, R. Golestanian, G. I. Guerrero-Garcia, M. Gruenwald, A. Haji-Akbari, M. Ibáñez, M. Karg, T. Kraus, B. Lee, R. C. van Lehn, R. J. Macfarlane, B. M. Mognetti, A. Nikoubashman, S. Osat, O. V. Prezhdo, G. M. Rotskoff, L. Saiz, A.-C. Shi, S. Skrabalak, I. I. Smalyukh, et al., *ACS Nano* **2024**, *18*, 14791.
[8] M. A. Boles, M. Engel, D. V. Talapin, *Chem. Rev.* **2016**, *116*, 11220.
[9] G. M. Grason, *Phys. Rep.* **2006**, *433*, 1.
[10] B. Nouri, H.-L. Chen, *J. Polym. Res.* **2024**, *31*, 120.
[11] A.-C. Shi, *J. Phys. Condens. Matter* **2021**, *33*, 253001.
[12] K. Kim, M. W. Schulze, A. Arora, R. M. Lewis, M. A. Hillmyer, K. D. Dorfman, F. S. Bates, *Science* **2017**, *356*, 520.
[13] S. Lee, C. Leighton, F. S. Bates, *Proc. Natl. Acad. Sci. USA* **2014**, *111*, 17723.
[14] C. R. Iacovella, A. S. Keys, S. C. Glotzer, *Proc. Natl. Acad. Sci. USA* **2011**, *108*, 20935.
[15] B. W. Goodfellow, Y. Yu, C. A. Bosoy, D.-M. Smilgies, B. A. Korgel, *J. Phys. Chem. Lett.* **2015**, *6*, 2406.
[16] H. Yun, Y. J. Lee, M. Xu, D. C. Lee, G. E. Stein, B. J. Kim, *ACS Nano* **2020**, *14*, 9644.
[17] B. W. Goodfellow, B. A. Korgel, *ACS Nano* **2011**, *5*, 2419.

[18] L. L. Missoni, M. Tagliazucchi, *ACS Nano* **2020**, *14*, 5649.
[19] K. Bian, J. J. Choi, A. Kaushik, P. Clancy, D.-M. Smilgies, T. Hanrath, *ACS Nano* **2011**, *5*, 2815.
[20] D. Gu, F. Schüth, *Chem. Soc. Rev.* **2014**, *43*, 313.
[21] R. P. Thedford, F. Yu, W. R. T. Tait, K. Shastri, F. Monticone, U. Wiesner, *Adv. Mater.* **2023**, *35*, 2203908.
[22] C. Li, Q. Li, Y. V. Kaneti, D. Hou, Y. Yamauchi, Y. Mai, *Chem. Soc. Rev.* **2020**, *49*, 4681.
[23] Y. Zou, X. Zhou, J. Ma, X. Yang, Y. Deng, *Chem. Soc. Rev.* **2020**, *49*, 1173.
[24] A. Saleem, Y. Zhang, M. Usman, M. Haris, P. Li, *Nano Today* **2022**, *46*, 101607.
[25] M. Vallet-Regí, F. Schüth, D. Lozano, M. Colilla, M. Manzano, *Chem. Soc. Rev.* **2022**, *51*, 5365.
[26] T. Tian, S. Yin, S. Tu, C. L. Weindl, K. S. Wienhold, S. Liang, M. Schwartzkopf, S. V. Roth, P. Müller-Buschbaum, *Adv. Funct. Mater.* **2021**, *31*, 2105644.
[27] G. Fleury, D. Hermida-Merino, D. Jingjin, K. Aissou, A. Bytchkov, G. Portale, *Adv. Funct. Mater.* **2019**, *29*, 1806741.
[28] R. Nagarajan, *J. Colloid Interface Sci.* **2015**, *449*, 416.
[29] X. Ke, M. Zhang, K. Zhao, D. Su, *Small Methods* **2022**, *6*, 2101040.
[30] V. Malgras, Y. Shirai, T. Takei, Y. Yamauchi, *J. Am. Chem. Soc.* **2020**, *142*, 15815.
[31] S. Kishimoto, Q. Wang, H. Xie, Y. Zhao, *Appl. Opt.* **2007**, *46*, 7026.
[32] D. Siliqi, L. de Caro, M. Ladisa, F. Scattarella, A. Mazzone, D. Altamura, T. Sibillano, C. Giannini, *J. Appl. Crystallogr.* **2016**, *49*, 1107.
[33] T. P. Lodge, C. L. Seitzinger, S. C. Seeger, S. Yang, S. Gupta, K. D. Dorfman, *ACS Polym. Au* **2022**, *2*, 397.
[34] Y. Ma, T. P. Lodge, *Macromolecules* **2016**, *49*, 9542.
[35] E. Wang, J. Zhu, D. Zhao, S. Xie, F. S. Bates, T. P. Lodge, *Macromolecules* **2020**, *53*, 417.
[36] E. G. Kelley, R. P. Murphy, J. E. Seppala, T. P. Smart, S. D. Hann, M. O. Sullivan, T. H. Epps, *Nat. Commun.* **2014**, *5*, 3599.
[37] Y.-S. Sun, Y.-Q. Jian, S.-T. Yang, P.-H. Chiang, C.-J. Su, *Soft Matter* **2025**, *21*, 277.
[38] S. H. Kim, M. J. Misner, T. Xu, M. Kimura, T. P. Russell, *Adv. Mater.* **2004**, *16*, 226.
[39] O. Dreyer, G. Ibbeken, L. Schneider, N. Blagojevic, M. Radjabian, V. Abetz, M. Müller, *Macromolecules* **2022**, *55*, 7564.
[40] M. G. Hennessy, G. L. Ferretti, J. T. Cabral, O. K. Matar, *J. Colloid Interface Sci.* **2017**, *488*, 61.
[41] L. Wu, X. Wang, G. Wang, G. Chen, *Nat. Commun.* **2018**, *9*, 1335.
[42] S. E. Kim, D. H. Kim, S. Y. Kim, *Adv. Funct. Mater.* **2022**, *32*, 2202690.
[43] D. H. Kim, S. Y. Kim, *ACS Nano* **2020**, *14*, 7140.
[44] M. W. Matsen, *Phys. Rev. Lett.* **1995**, *74*, 4225.
[45] M. J. Park, J. Bang, T. Harada, K. Char, T. P. Lodge, *Macromolecules* **2004**, *37*, 9064.
[46] L.-T. Chen, C.-Y. Chen, H.-L. Chen, *Polymer* **2019**, *169*, 131.
[47] A. Jayaraman, D. Y. Zhang, B. L. Dewing, M. K. Mahanthappa, *ACS Cent. Sci.* **2019**, *5*, 619.
[48] Y. Ma, H. T. Davis, L. E. Scriven, *Prog. Org. Coat.* **2005**, *52*, 46.
[49] J. Zhou, X. Man, Y. Jiang, M. Doi, *Adv. Mater.* **2017**, *29*, 1703769.
[50] L. Q. Wagner, E. Da Prates Costa, C. Glatthaar, F. Breckwoldt, M. Zecca, P. Centomo, X. Huang, C. Kübel, H. Schlaad, M. Kriechbaum, H. Amenitsch, M. Thommes, B. M. Smarsly, *Chem. Mater.* **2023**, *35*, 9879.
[51] F. A. Jung, A. V. Berezkin, T. B. Tejsner, D. Posselt, D.-M. Smilgies, C. M. Papadakis, *Macromol. Rapid Commun.* **2020**, *41*, 2000150.
[52] C. Sinturel, M. Vayer, M. Morris, M. A. Hillmyer, *Macromolecules* **2013**, *46*, 5399.
[53] D. Posselt, J. Zhang, D.-M. Smilgies, A. V. Berezkin, I. I. Potemkin, C. M. Papadakis, *Prog. Polym. Sci.* **2017**, *66*, 80.
[54] S.-M. Yang, J. Oh, B. R. Magruder, H. J. Kim, K. D. Dorfman, M. K. Mahanthappa, C. J. Ellison, *Phys. Rev. Mater.* **2023**, *7*, 125601.
[55] R. Meier, H.-Y. Chiang, M. A. Ruderer, S. Guo, V. Körstgens, J. Perlich, P. Müller-Buschbaum, *J. Polym. Sci. B: Polym. Phys.* **2012**, *50*, 631.
[56] Y.-S. Sun, S.-W. Chien, J.-Y. Liou, *Macromolecules* **2010**, *43*, 7250.
[57] J. Lee, M. C. Orilall, S. C. Warren, M. Kamperman, F. J. DiSalvo, U. Wiesner, *Nat. Mater.* **2008**, *7*, 222.
[58] Y. Ren, Y. Zou, Y. Liu, X. Zhou, J. Ma, D. Zhao, G. Wei, Y. Ai, S. Xi, Y. Deng, *Nat. Mater.* **2020**, *19*, 203.
[59] W. Xie, X. Huang, C. Zhu, F. Jiang, Y. Deng, B. Yu, L. Wu, Q. Yue, Y. Deng, *Adv. Mater.* **2024**, *36*, 2313920.
[60] A. Kar, S. Kundu, A. Patra, *J. Phys. Chem. C* **2011**, *115*, 118.
[61] C. Zhang, J. Lin, *Chem. Soc. Rev.* **2012**, *41*, 7938.
[62] S. Das, V. Jayaraman, *Prog. Mater. Sci.* **2014**, *66*, 112.
[63] M. Batzill, U. Diebold, *Prog. Surf. Sci.* **2005**, *79*, 47.
[64] L. Z. Liu, T. H. Li, X. L. Wu, J. C. Shen, P. K. Chu, *J. Raman Spectrosc.* **2012**, *43*, 1423.
[65] J. Hu, Y. Zou, Y. Deng, H.-J. Li, H. Xu, D. Wang, L. Wu, Y. Deng, G. Li, *Prog. Mater. Sci.* **2025**, *150*, 101409.
[66] Y. Masuda, *Sens. Actuators, B* **2022**, *364*, 131876.
[67] J. Wu, S. Feng, X. Wei, J. Shen, W. Lu, H. Shi, K. Tao, S. Lu, T. Sun, L. Yu, *Adv. Funct. Mater.* **2016**, *26*, 7462.
[68] T. Le Duy, D.-J. Kim, T. Q. Trung, V. Q. Dang, B.-Y. Kim, H. K. Moon, N.-E. Lee, *Adv. Funct. Mater.* **2015**, *25*, 883.
[69] W. Zhang, J. Liu, Z. Jin, *ACS Appl. Nano Mater.* **2023**, *6*, 11802.